Journal of *Marine Science and Engineering*

MDPI

Article

Research on the Hydrodynamic Noise Characteristics of a Mixed-Flow Pump

Qiaoyue Yang [1], Wei Li [1,2,*], Leilei Ji [1,3,4], Weidong Shi [5], Wei Pu [1], Yu Long [1] and Xinrui He [1]

[1] National Research Center of Pumps, Jiangsu University, Zhenjiang 212013, China; 2222211043@stmail.ujs.edu.cn (Q.Y.); 2222211033@stmail.ujs.edu.cn (Y.L.); 2222211039@stmail.ujs.edu.cn (X.H.)
[2] Zhenjiang Fluid Engineering Equipment Technology Research Institute, Jiangsu University, Zhenjiang 212009, China
[3] Key Laboratory of Fluid and Power Machinery, Xihua University, Ministry of Education, Chengdu 610039, China
[4] Wenling Fluid Machinery Technology Institute, Jiangsu University, Wenling 317525, China
[5] College of Mechanical Engineering, Nantong University, Nantong 226019, China
* Correspondence: lwjiangda@ujs.edu.cn

Abstract: This study presents a comprehensive investigation of the internal noise characteristics of a mixed-flow pump by combining computational fluid dynamics (CFD) and computational acoustics. The turbulent flow field of the pump is simulated using the unsteady SST k-ω turbulence model in CFD. The contributions of the volute, guide vanes, and impeller to the internal noise are analyzed and compared using the Lighthill theory, FW-H formula, and LMS Virtual Lab software for acoustic simulation. The research findings indicate that the energy of pressure fluctuations in the mixed-flow pump is predominantly concentrated at the blade passing frequency and its low-frequency harmonics. This suggests that the internal noise is mainly in the low-frequency range, with higher energy at the blade passing frequency and its harmonics. Under the $0.6Q_{des}$ flow condition, the flow inside the pump becomes more complex, resulting in higher sound pressure levels and sound power levels compared to higher flow conditions. However, for flow conditions ranging from $0.8Q_{des}$ to $1.2Q_{des}$, the sound pressure levels gradually increase with increasing flow rate, with the sound pressure level at $1.0Q_{des}$ being nearly identical to that at $1.2Q_{des}$. The analysis of sound power level spectra at different flow rates reveals that the distribution characteristics of internal vortex structures directly impact the hydrodynamic noise inside the mixed-flow pump. These research findings provide a significant theoretical basis for noise control in mixed-flow pumps.

Keywords: mixed-flow pump; hydrodynamic noise; sound pressure level; numerical simulation

Citation: Yang, Q.; Li, W.; Ji, L.; Shi, W.; Pu, W.; Long, Y.; He, X. Research on the Hydrodynamic Noise Characteristics of a Mixed-Flow Pump. *J. Mar. Sci. Eng.* **2023**, *11*, 2209. https://doi.org/10.3390/jmse11122209

Academic Editor: María Isabel Lamas Galdo

Received: 8 November 2023
Revised: 15 November 2023
Accepted: 16 November 2023
Published: 21 November 2023

1. Introduction

The mixed-flow pump combines the advantages of centrifugal pumps and axial flow pumps and has been widely used in various industrial and agricultural fields. The internal working medium of the pump is mostly water or other liquids, while the external medium is often air. Due to the significant difference in the acoustic characteristics between these two fluid media, the acoustic field of the mixed-flow pump is commonly divided into the internal acoustic field and the external acoustic field. The corresponding hydrodynamic noise is referred to as the internal field noise and the external field noise, respectively. Based on the spectral distribution characteristics of the noise, hydrodynamic noise can also be classified into discrete noise caused by dynamic and static interference and vortex shedding as well as broadband noise generated by cavitation and turbulent fluctuations [1]. This paper primarily focuses on the investigation of discrete noise.

Discrete noise in the mixed-flow pump primarily manifests as noise at the pump shaft frequency, blade passing frequency, and their harmonics. Extensive research has been

conducted both domestically and internationally on discrete noise in turbomachinery in the field of aerodynamic noise. It is generally recognized that the main sources of discrete noise in turbomachinery include the strong dynamic and static interference between the wake of the internal impeller rotor and the guide vanes, volute tongue, and other stationary components as well as the phenomenon of vortex shedding when the laminar boundary layer passes over the trailing edge of the blades, resulting in intense fluctuation of surface pressure and the generation of discrete tonal noise [2]. Jui-Hsiang Kao et al. [3] used a combination of the CFD method and linear wave theory to solve the dipole noise of marine propeller radiation. Qin Wu et al. [4] predicted loading noise and cavitation noise based on the fan source theory and spherical bubble acoustic radiation theory, respectively. The study shows that in the non-cavitation case, the high sound pressure level is mainly concentrated in the low frequency level, which is reduced from the low order blade passing frequency to the high order blade passing frequency. In the case of plate cavitation, the sound pressure level is enhanced at the higher order of blade passing frequency. The sound pressure caused by cavitation development changes with the periodic change of the pulsating cavity, and the sound energy is mainly concentrated in the lower order of the blade passing frequency. Shuaikang Shi et al. [5] numerically simulated the structural noise and flow noise of a pump-jet propulsion submarine at low speed. The results show that the peak value of the SUBOFF structure noise is the characteristic frequency of the longitudinal mode of the shafting system, in-phase mode of the rotor blade, and pulsating pressure. Due to the interaction of the rotating rotor, the main peak of the sound pressure level of the flow noise is the same as the pulsating pressure. Jiaming Yu et al. [6] applied PIV and the proposed wavelw-based beamforming method to study the flow fluctuations, transient flow dynamics, and their correlations in the experimental study of trailing edge noise. It was found that vortex separation and boundary layer instability are the sources of trailing noise at lower and higher Reynolds numbers, respectively. Cavitation and external mechanical vibrations can also contribute to the noise in mixed-flow pumps. The research conducted by Michał Stosiak et al. [7] reveals that external mechanical vibrations have a significant impact on hydraulic valves in various military hydraulic drive systems. They introduced passive vibration isolation, and the reduction in pressure pulsations resulted in decreased vibration levels in the hydraulic system, lower noise emissions during operation, and a more stable operation of the hydraulic receiver.

Currently, there is a considerable amount of research on hydrodynamic noise in centrifugal pumps in China. The studies on internal discrete noise mainly focus on reducing the noise generated by the dynamic and static interference between the impeller and the stationary components. Rajavamsi Gangipamula et al. [8] investigated the correlation between flow noise and air noise of the centrifugal pump through an experimental and numerical study of a double suction impeller volute pump. It was found that the volute tongue has a great influence on the flow noise and air noise of the centrifugal pump. In the study conducted by Zheng Yuan [9], it was indicated that under different operating conditions, the dominant frequency of pressure fluctuations throughout the mixed-flow pump remains consistent with the blade passing frequency. The dynamic and static interference between the impeller and the volute in the mixed-flow pump is the main cause of flow-induced noise. The dominant frequency of flow-induced noise is determined by a combination of the dominant frequency of pressure fluctuations and the inherent frequency of the pump structure. Under different operating conditions, the stronger the pressure fluctuations inside the mixed-flow pump, the higher the level of flow-induced noise radiation corresponding to that particular operating condition. Fu Jian [10] combined the boundary element method and point source model theory to complete the numerical calculation and result verification of static wall flow noise and rotating sound source noise under arbitrary boundary conditions. The results show that the amplitude of the pulsating pressure on the stationary wall of the mixed-flow pump is strongest in the interaction area between the impeller and the guide vane. The peak noise frequency corresponding to the stationary component is mainly in the blade frequency, the guide vane passing frequency,

and the harmonic frequency of the two. The noise caused by the impeller at the inlet section of the mixed flow pump is the main component, and the contribution of the stationary parts can be ignored. Lang Tao [11,12] and other researchers employed a combination of computational fluid dynamics and computational acoustics to investigate the acoustic source characteristics and aerodynamic noise characteristics induced by cavitation in the internal flow field of a single-blade pump under different flow rate conditions. The research results indicate that the energy of pressure fluctuations is mainly concentrated at the blade passing frequency and its low-frequency harmonics. The energy of internal noise is primarily concentrated in the low-frequency range, with higher energy levels at the blade passing frequency and its harmonics. As the flow rate increases, the occurrence of secondary flows and flow separation between the volute and the impeller passage decreases, leading to a significant decrease in the harmonics noise in the low-frequency range. Han Wei [13] found that the contribution of the external field noise in a helical mixed-flow pump decreases in the following order: casing, impeller, and guide vanes. Moreover, with an increase in the flow rate, the noise from each passage component gradually decreases. Luo [14] investigated the vibration characteristics of nuclear centrifugal pumps at low flow rates. The results showed that the vibration frequencies were concentrated in the low-frequency range from 0.23 times of the rotational frequency to 0.25 times of the rotational frequency. At low flow rates, the pump blade frequency is highly sensitive to hydraulic disturbances, leading to an increase in vibration frequencies, including the rotational frequency and twice the rotational frequency. Lu et al. [15] conducted a study on the linear startup process of a mixed-flow pump using a synchronized data acquisition experimental system. They found that during rapid startups with varying acceleration times, a strong acceleration corresponding to a short acceleration time would suppress impeller cavitation. Li et al. [16] developed theoretical methods for calculating the head and estimating the transient energy conversion efficiency during the startup process of a mixed-flow pump. They combined the pipeline characteristic equation to solve for the transient flow rate, head, and other hydraulic performance parameters during the pump startup process. The transient characteristics under linear and exponential startup modes were analyzed. Si et al. [17] investigated the coupling mechanism between the ducted-propeller (DP) flow field and the acoustic field and developed a three-dimensional flow-acoustic coupling numerical model based on the vortex acoustics equation. By combining simulation and experimental research, they studied the unsteady flow field of the DP configuration. The generation mechanism of sound waves and the distribution characteristics of the acoustic field were examined, and the propagation behavior of fluid dynamic noise caused by the DP was analyzed based on the theory of field synergy. Zhu Guojun et al. [18] investigated the variation patterns and influencing factors of noise in a mixed-flow pump under different startup modes. It was found that high-amplitude sound pressure occurred in the later stages of startup under all modes. Among them, the concave exponential function startup mode exhibited the shortest duration of high-amplitude noise occurrence and relatively minimal impact noise. This indicates that this startup mode is advantageous in avoiding severe mechanical collisions and impacts during the startup process. With the continuous advancement in technology, simulation and modeling techniques have become increasingly sophisticated. The utilization of updated numerical simulation methods can enhance the accuracy of results. In the study conducted by Karpenko et al. [19], the authors employed 3D Reynolds-averaged Navier-Stokes (RANS) equations for numerical simulations to analyze the influence of hydrodynamic processes on the fluid flow characteristics in a pipeline system with installed elbow fittings.

In this study, a combination of computational fluid dynamics and computational acoustics was employed to investigate the internal noise of a mixed-flow pump. The aim was to explore the acoustic source characteristics of the internal flow field and compare the noise differences between stationary and rotating components within the mixed-flow pump. Through this research, a deeper understanding of the mechanisms and characteristics of

hydrodynamic noise in mixed-flow pumps was gained, providing valuable theoretical foundation and practical guidance for noise control in mixed-flow pumps.

2. Materials and Methods

2.1. Sound Field Solving Theory

Similar to aerodynamic noise, hydrodynamic noise is an interdisciplinary field that combines unsteady fluid dynamics and acoustics [20]. Currently, in the research of hydrodynamic noise, theoretical methods and tools predominantly originate from aerodynamic acoustics, with the exclusion of cavitation noise in water. Therefore, both domestic and international scholars generally classify hydrodynamic noise and aerodynamic noise under the discipline of aerodynamic acoustics.

The research in aerodynamic acoustics is widely acknowledged to have originated from Lighthill. In 1952, Lighthill [21] introduced the acoustic analogy method and Lighthill equation, as shown in Equation (1):

$$\begin{cases} \frac{\partial^2(\rho-\rho_0)}{\partial t^2} - c_0^2\nabla^2(\rho-\rho_0) = \frac{\partial^2 T_{ij}}{\partial x_i \partial x_j}, \\ T_{ij} = \left[\rho u_i u_j + \delta_{ij}\left[(p-p_0) - c_0^2(\rho-\rho_0)\right] - \delta_{ij}\right], \end{cases} \tag{1}$$

where ∇ represents the Hamilton operator, $\nabla = \vec{i}\frac{\partial}{\partial y_1} + \vec{j}\frac{\partial}{\partial y_2} + \vec{k}\frac{\partial}{\partial y_3}$; ρ represents the fluid density, kg/m^3; ρ_0 represents the reference density, kg/m^3; t represents time, s; c_0 is the speed of sound, m/s; T_{ij} refers to the Lighthill stress tensor; x represents the spatial coordinates, with subscripts i and j denoting the components along the coordinate axes, following the summation convention of tensors; u represents the fluid velocity, m/s; p represents the pressure exerted on the fluid, Pa; p_0 represents the undisturbed pressure experienced by the fluid, Pa; and δ_{ij} is the unit tensor, $\delta_{ij} = \begin{cases} 0 (i \neq j) \\ 1 (i = j) \end{cases}$.

The acoustic analogy method, as envisioned in Lighthill's work, assumes that the sources of sound in the flow field are independent and that sound propagation is unaffected by the fluid. By manipulating the N-S equations, one can derive the wave equation for sound in the fluid. Lighthill focused on free-field sound radiation and did not extend the integral solution form. To obtain the complete integral form solution of the Lighthill equation, Curle [22] employed the Kirchhoff integral method, considering the influence of solid obstacles on the surface of the fluid. Curle derived the Curle equation, as shown in Equation (2):

$$\rho(x,t) = \frac{1}{4\pi c_0^2}\int_V \frac{\partial^2 T_{ij}}{\partial y_i \partial y_j}\left(y, t - \frac{r}{c_0}\right)dy + \frac{1}{4\pi c_0^2}\int_S \frac{\partial\left(l_j \tau_{ij}\right)}{\partial y_i \partial y_j}\left(y, t - \frac{r}{c_0}\right)dy \tag{2}$$

where τ_{ij} is the viscous stress tensor; r is the distance between the field point and the source point, $r = |x - y|$; x represents the field point; and y represents the source point.

Williams et al. [23] extended the Kirchhoff integral method to incorporate moving solid boundaries, thereby providing the most general form of the Lighthill acoustic analogy known as the FW-H equation. It is expressed by Equation (3):

$$\begin{cases} \frac{\partial^2 H(f)\rho}{\partial t^2} - c_0^2\nabla^2[\rho H(f)] = \frac{\partial^2\left[T_{ij}H(f)\right]}{\partial x_i \partial x_j} + \frac{\partial F_i \delta(f)}{\partial x_i} + \frac{\partial Q\delta(f)}{\partial t} \\ F_i = -[\rho u_i(u_j - v_j) + p\delta_{ij} - \tau_{ij}]\frac{\partial f}{\partial x_i} \\ Q_i = [\rho(u_j - v_j) + \rho_0 v_j]\frac{\partial f}{\partial x_i} \end{cases} \tag{3}$$

where $\delta(f)$ is the Dirac delta function; $H(f)$ is the Heaviside function; u_i is the component of fluid velocity; v_i is the component of surface velocity; t is time, s; and n_i represents the unit normal vector along the exterior normal to the surface of the sound source.

By performing the integration of Equation (3), we obtain:

$$\begin{aligned} H(f)\rho(x,t) = \; & \frac{1}{4\pi c_0}\int_V \frac{\partial}{\partial y_i \partial y_j}\left[\frac{1}{|1-M_r|}T_{ij}\left(y, t-\frac{r}{c_0}\right)\right]\frac{dy}{r} \\ & + \frac{1}{4\pi c_0}\int_\Sigma \frac{\partial}{\partial y_i}\left[\frac{1}{|1-M_r|}F_i\left(y, t-\frac{r}{c_0}\right)\right]\frac{dy}{r|\nabla f|} \\ & + \frac{1}{4\pi c_0}\int_\Sigma \frac{\partial}{\partial t}\left[\frac{1}{|1-M_r|}Q_i\left(y, t-\frac{r}{c_0}\right)\right]\frac{dy}{r|\nabla f|} \end{aligned} \tag{4}$$

where M_r is the Mach number of the moving source in the direction of the observer.

In Equation (4), the first term on the right-hand side represents the Lighthill acoustic source, which signifies the contribution of quadrupole sources to the acoustic field. The second term represents the pressure fluctuations within the boundary layer of the solid wall motion, indicating the contribution of dipole sources in the flow field to the acoustic field. The third term represents the interaction between the solid wall motion and the flow field, representing the contribution of monopole sources in the flow field to the acoustic field. Directly solving the FW-H equation is challenging, and early solution methods involved solving the FW-H equation in the frequency domain. However, these methods were infrequently used due to the complexity of the computational formulas. Subsequently, with the continuous improvement of computer performance, Farassat [24] proposed a time-domain solution for the FW-H equation. By introducing the Green's function formula and adjusting the FW-H equation, Farassat derived time-domain integral expressions for monopole and dipole noise sources. Farassat's time-domain solution method enabled the widespread application of the FW-H equation in the engineering field.

Goldstein [25] proposed a generalized form of the Lighthill equation for solving the sound generation problem in homogeneous moving media. The various methods based on Lighthill's ideas mentioned above are collectively referred to as the acoustic analogy methods. Bailly [26] analyzed plate noise using two methods: direct noise computation (DNC) and the acoustic analogy theory. The results showed that the acoustic analogy theory provided comparable results to DNC calculations at low Mach numbers, but with higher computational efficiency. Lighthill emphasized the compressible nature of fluids as an essential factor for sound propagation, which is why he incorporated density variations as an acoustic quantity in his equations. With the development of aeroacoustics, researchers have proposed various acoustic analogy equations based on different acoustic quantities, depending on their specific research areas. Powell [27] introduced vorticity into the Lighthill equation and derived the Powell equation, as shown in Equation (5):

$$\nabla^2 p - \frac{1}{c_0^2}\frac{\partial^2 p}{\partial t^2} = -\nabla \cdot [\rho(\omega \times u)] \tag{5}$$

where ω represents vorticity; u is the velocity vector of fluid particles; and $\omega \times u$ represents the acoustic source, where a larger vorticity leads to a greater noise generation.

Powell developed the vorticity acoustic theory, which uses the magnitude of vorticity as a measure of acoustic source energy. He pointed out that for low Mach numbers in adiabatic and isentropic fluids, both fluid motion and sound radiation are generated by vorticity. The vorticity acoustic theory proposed by Powell is essentially an extension of Lighthill's theory for low Mach numbers.

Howe [28] further developed the vortex sounding theory by considering the effect of entropy change and mean flow on flow sounding and proposed Howe's equation, as shown in Equation (6):

$$\left\{\frac{D}{Dt}\left(\frac{1}{c_0^2}\frac{D}{Dt}\right)+\frac{1}{c_0^2}\frac{Du}{Dt}\nabla-\nabla^2\right\}B=$$
$$\nabla\cdot\{\omega\times u-T\nabla s\}-\frac{1}{c_0^2}\frac{Du}{Dt}\{\omega\times u-T\nabla s\}+\frac{1}{c_p}\left\{\frac{\partial}{\partial t}\frac{Ds}{Dt}+\frac{1}{\gamma-1}\frac{D^2s}{Dt^2}\right\} \quad (6)$$

where D is the Doppler amplification factor, $D = |1 - M_r|$; E is the internal energy of the fluid; T is the temperature, K; s is the entropy; B denotes the stagnation enthalpy of the fluid, defined as $E + \frac{P}{\rho} + \frac{u^2}{2}$; c_p is the specific heat capacity of pressure; c_v is the specific heat capacity of constant volume; and γ is the ratio of specific heat, defined as $\frac{c_p}{c_v}$.

The Powell equation can be regarded as a modification of the Howe equation under the condition of low Mach numbers. Subsequently, Howe [29] pointed out in his research that the transient pressure on solid surfaces is the primary cause of noise generation. He proposed a research approach that involves first calculating the flow field and then computing the sound field for studying the rotationally induced sound field by machinery. Timushev [30] and others utilized the vorticity acoustic theory to solve the flow-induced noise within a centrifugal pump, and the results demonstrated good agreement with experimental data. In addition to Howe, several researchers [31–34] have investigated the aerodynamic noise mechanisms from different perspectives. The studies indicate that there exist interactions and correlations between acoustic waves, fluid vortices, and different vortices. According to the acoustic analogy theory, turbulent noise exhibits quadrupole source characteristics. For mixed-flow pumps, the Mach number of the internal flow is less than 1, which means that turbulent sound waves cannot reach the far field. However, during the dynamic and static interference between turbulence and the impeller, volute, and guide vanes of the pump, the quadrupole sources undergo scattering. This leads to intense pressure fluctuations on the surfaces of the rotor or stator, resulting in the generation of dipole sources and increased radiation efficiency. Therefore, in numerical simulation studies, the contribution of dipole sources to the sound field is often considered.

2.2. Numerical Calculation Model and Method

2.2.1. Flow Field Calculation Model and Grid Division

The research object of this study is a low specific speed mixed-flow pump with guide vanes. The computational domain covers the entire device section from the inlet section of the pump to the outlet section of the annular volute, as shown in Figure 1. The design parameters are as follows: rated flow rate Q_{des} = 380 m^3/h, rated head H = 6 m, rated speed n = 1450 r/min, specific speed n_s = 480, number of impeller blades Z = 4, and number of guide vane blades Z_d = 7. The inlet diameter of the pump is D_1 = 250 mm, the outlet diameter is D_2 = 200 mm, and the blade tip clearance is δ = 0.2 mm.

The physical model of the mixed-flow pump includes six parts: inlet section, impeller section, guide vane section, annular worm chamber section, and outlet section, with a large spatial structure. Therefore, the inlet section, impeller section, guide vane section, worm chamber section, and outlet section of the mixed-flow pump model are discretized separately during meshing, and in order to obtain more accurate results of the flow field, high-quality hexahedral structured meshes are drawn for all the computational domains. Among them, the water body domain inside the impeller section adopts the J/O type topology; in order to ensure that there are enough meshes in the gap of the blade rim, the mesh encryption process is realized by increasing the mesh nodes in the gap and at the same time adjusting the mesh scale in the near-wall area, controlling that the mesh Y^+ value of the gap area varies in the range of 100; Y^+ is the dimensionless coefficient representing the boundary layer mass. The mesh of each part of the mixed-flow pump is shown in Figure 2. The number of grids in each part of the computational domain, inlet section,

impeller section, guide vane section, annular worm chamber section, and the total number of grids are 246,048, 2,827,416, 2,298,345, 437,091, and 5,808,900, respectively.

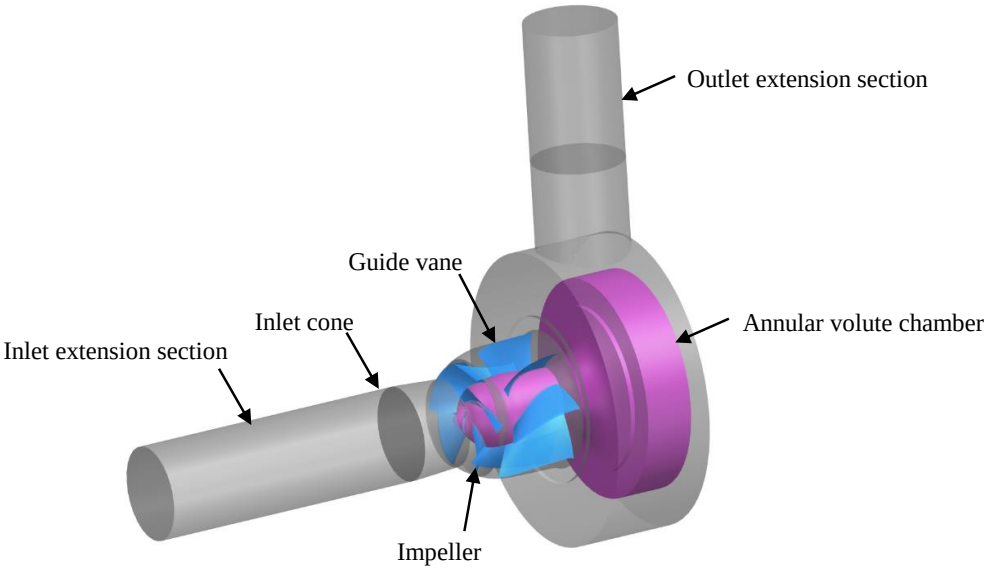

Figure 1. Three-dimensional model of mixed-flow pump.

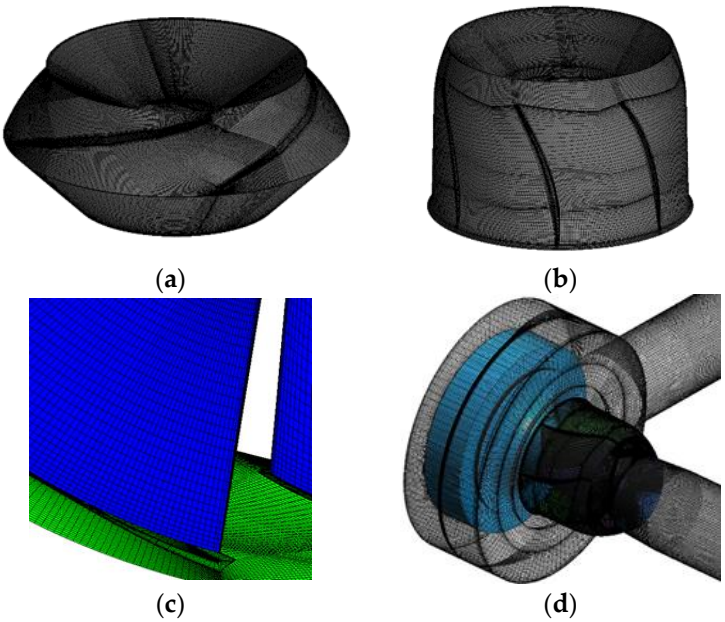

Figure 2. Mesh of computational domains: (**a**) impeller mesh; (**b**) guide vane mesh; (**c**) blade tip region mesh; (**d**) mixed-flow pump mesh.

In the process of numerical calculation of mixed-flow pump, it is necessary to quantitatively analyze the errors in numerical calculation, the causes of errors, and the influence range. In particular, the density and quality of the mesh largely determine the accuracy and reliability of the simulation. In order to take into account the accuracy and efficiency of the calculation, it is usually necessary to carry out grid independence verification before numerical calculation to determine the appropriate number of grids.

In this paper, by adjusting the number and position of grid nodes in the topology structure, 5 sets of structural grids with different grid numbers are obtained. The numerical calculation of 5 different quantities of grids under rated working conditions is carried out, and the pump head and efficiency are compared as reference standards, and the

results are shown in Figure 3. When the total grid number of the model is greater than 5.8 million, its head and efficiency are basically unchanged, which meets the requirement of the grid independence test. Therefore, considering the calculation accuracy and efficiency, a grid scheme with an overall grid number of 5.8 million was selected for the subsequent numerical calculation study.

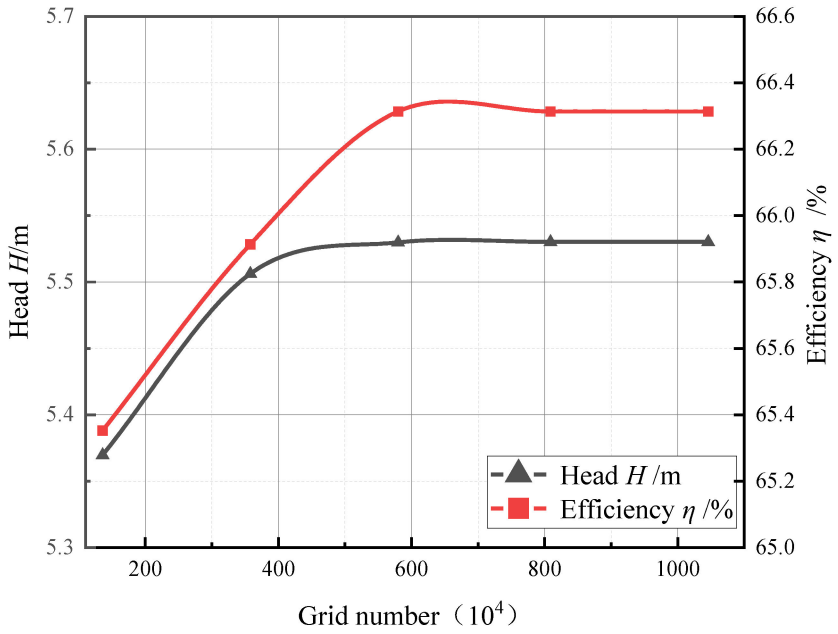

Figure 3. Variation trends of head and efficiency with different grid numbers.

2.2.2. Flow Field Calculation of Turbulence Model and Boundary Conditions

Based on ANSYS CFX, following the ITTC-CFD Uncertainty Analysis Guidelines, the SST k-ω turbulence model was selected for the model after validation. In the steady-state flow analysis, four operating conditions were considered: $0.6Q_{des}$, $0.8Q_{des}$, $1.0Q_{des}$, and $1.2Q_{des}$. For the unsteady flow analysis, the steady-state flow field results of the four flow rate conditions were used as initial conditions to simulate and solve the unsteady flow conditions inside the mixed-flow pump at the four operating points. In the numerical simulation, a multiple reference frame (MRF) approach was employed. The impeller domain was set as a rotating domain, while the remaining fluid domains were considered stationary. For steady-state simulations, data transfer between the stationary and rotating domains was accomplished using a frozen-rotor interface, while for unsteady simulations, a sliding mesh technique was utilized through a transient rotor/stator interface. The medium used in the simulations was clean water at a temperature of 25 °C. The solid walls of the entire computational domain were assigned as no-slip walls. The inlet boundary condition was specified as total pressure inlet, while the outlet boundary condition was set as a flow rate outlet.

Considering computation time and accuracy, in the steady-state simulations, the solver settings were kept consistent for all flow rate conditions. The time step size was set to 0.00025, the number of iterations per step was set to 2000, and the convergence criterion was set to 10^{-4}. In the unsteady simulations, a time step size of 3° per step was used, which was sufficient to capture dynamic pressure signals. The impeller completed 10 revolutions, resulting in a total of 1600 time steps. The convergence criterion for the unsteady simulations was also set to 10^{-4}. The calculation was considered converged when the monitored values exhibited periodic stability. For the analysis of the unsteady flow field, data extraction was performed starting from the 5th revolution, and a total of 5 revolutions' worth of data were extracted.

2.2.3. Noise Numerical Simulation Methods

There are three main approaches for fluid acoustic simulation: direct numerical simulation, acoustic field prediction based on semi-empirical models, and hybrid numerical simulation. Among them, hybrid numerical simulation is the most commonly used in scientific research and engineering. The basic idea is to first use computational fluid dynamics (CFD) methods to obtain the internal flow field of the pump. Then, the temporal pressure fluctuation information in the flow field is converted into sound source information. Finally, by neglecting fluid viscosity, the acoustic field is predicted based on the acoustic wave propagation equation or acoustic analogy methods. Since the acoustic energy is much smaller than the fluid energy, this method does not consider the effect of the acoustic field on the flow field.

This study focuses on the contribution of pump wall dipole sources to the acoustic field. In rotating machinery, dipole sources include the guide vane, volute casing wall dipole, and impeller wall rotating dipole. Different computational approaches are used for these sources. In this paper, the guide vane and volute casing wall dipoles are referred to as stationary component dipoles, while the impeller wall dipole is referred to as the rotating component dipole. Figure 4 illustrates the calculation approach for the noise generated by the stationary and rotating component dipoles. The acoustic field calculations were performed using the Acoustic module in LMS Virtual Lab. For both types of dipole sources, the internal acoustic field was obtained using the finite element method (FEM) in acoustics, including the distribution of flow-induced noise and sound power within the mixed-flow pump.

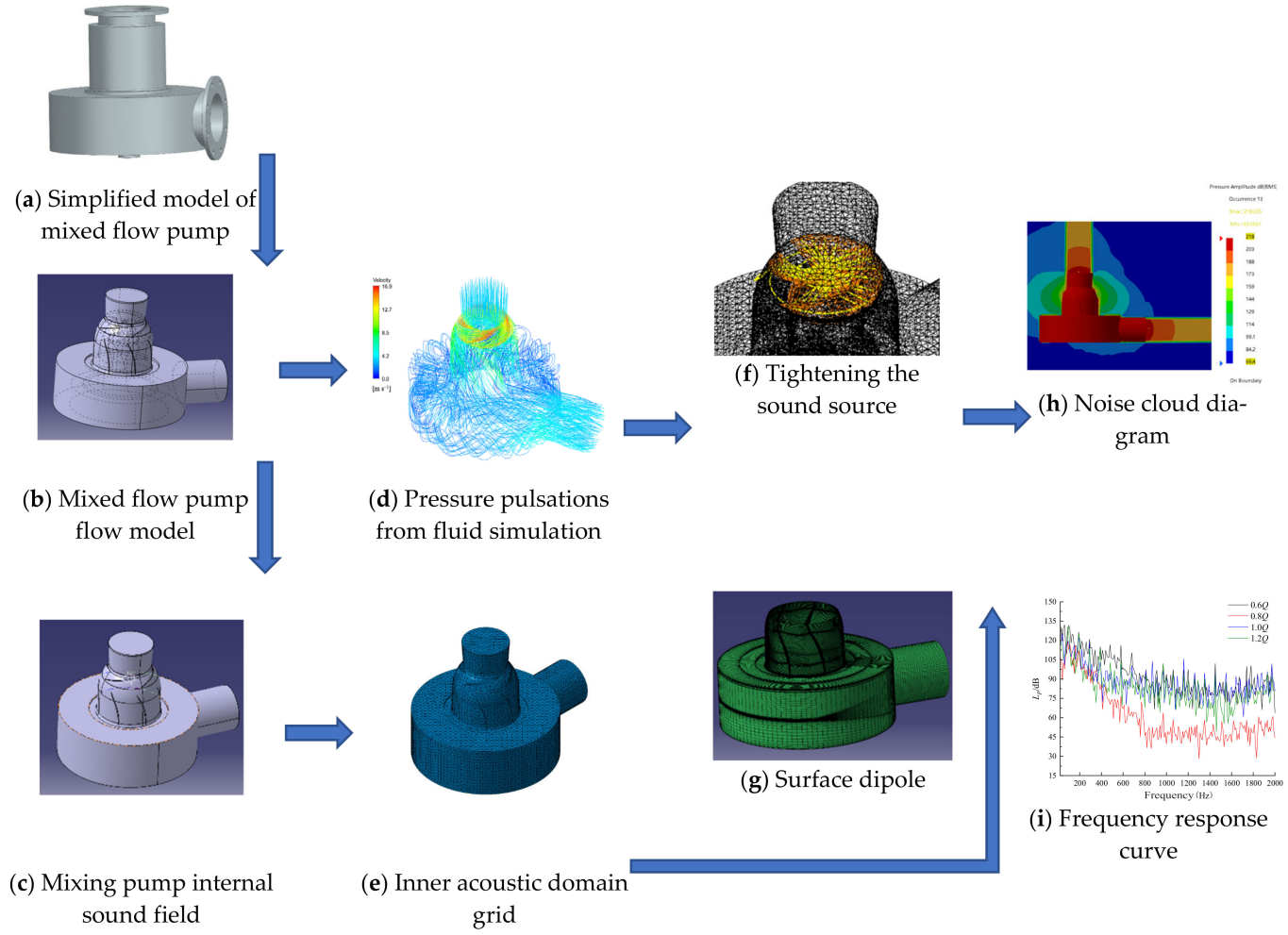

Figure 4. Flow of dipole noise calculation.

2.2.4. Stationary Component Dipole Noise

Figure 4e shows the acoustic finite element mesh, which has been coarsened. The size of the mesh elements needs to strictly adhere to the criterion that the number of grid cells per wavelength should be greater than 6. The wavelength is determined based on the highest frequency. In this numerical simulation, the mesh consists of 128,014 elements and 28,125 nodes, which adequately meet the requirements for acoustic field simulation calculations.

An important step in the calculation of the volute casing wall dipole acoustic field is pressure data mapping, which involves mapping the pressure data stored at the CFD grid nodes onto the acoustic grid as boundary conditions for sound propagation calculations. Therefore, the conservative maximum distance algorithm is used to compute the data mapping process, reducing energy losses during the mapping process. Additionally, following the frequency-domain calculation approach for sound propagation, the temporal pressure fluctuation data need to be Fourier-transformed during the data mapping process, converting the temporal signal of fluid pressure into frequency-domain data. The pressure fluctuation data from the 5th to the 10th revolution in the CFD simulation are used as the source signals. The inlet and outlet surface of the pump are set to have the AML attribute, while the inner wall surface of the volute casing grid is set as a fully reflective wall. Other parameter settings for sound propagation calculations are presented in Table 1.

Table 1. Settings for calculating the sound field inside the dipole of a stationary component.

Sound Propagation Calculation Module	Acoustical Finite Element (FEM)
CFD sound sources information	Laps 5–10 pulsating pressure data
CFD maximum analysis frequency $f_{max\text{-}cfd}$	2000 Hz
CFD frequency resolutions $\triangle f_{cfd}$	5.0 Hz
Fluid media	Water
Density ρ_{water}	997 kg/m^3
Velocity c_{water}	1500 m/s
AML	Inlet and outlet of the pump
Fully reflective wall	Mesh of wall surfaces inside stationary parts
Maximum analyzed frequency for sound field calculation $f_{max\text{-}aco}$	2000 Hz
Frequency resolution of sound field calculations $\triangle f_{aco}$	5.0 Hz

2.2.5. Rotating Component Dipole Noise

According to the FW-H theory, the noise generated by the rotating dipole is simulated, and it is converted into pressure fluctuations acting as blade loads, as shown in Figure 5. When defining the sound source boundary conditions for the rotating dipole, all the surface elements in the CFD grid are simplified into a single point source. This point source contains the temporal signal information of the pressure fluctuations. Additionally, the equivalent source method is employed to compactly represent the rotating dipole as a compact sound source. The impeller is divided into segments, where each segment can be considered as a compact sound source relative to the wavelength of the sound wave. The loads on the surface of each segment are integrated to the centroid of that segment, resulting in the total load on the impeller. To obtain wideband noise, the temporal pressure fluctuation signals at each point are divided into equal duration segments. In the subsequent acoustic calculations, the calculation of wideband noise is achieved by setting the impeller speed and the number of subharmonics. To ensure that the impeller dipole noise spectrum has the same frequency resolution as the volute casing dipole noise spectrum, this study adopts a total duration of 5 revolutions as one time segment. The settings for the rotating dipole sound source definition are presented in Table 2. For the configuration of other acoustic finite element meshes and field point grids, please refer to Table 1.

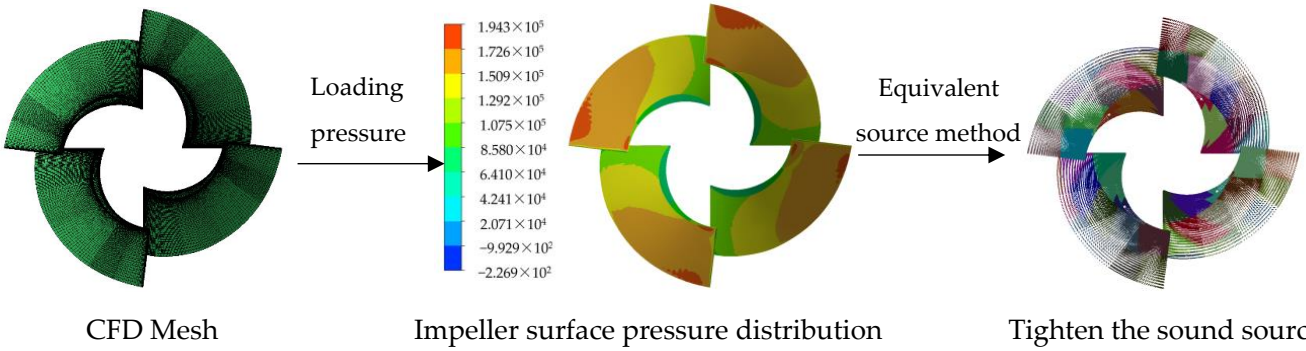

Figure 5. Generating a tight sound source.

Table 2. Calculated sound field setup inside the rotating component dipole.

Duration of the Segment	Five Laps
Block overlap	0%
Number of time periods	1
Rotational speed of impeller	1450 r/min
Calculate the harmonic frequency order	18
Number of subharmonic frequencies	4

2.2.6. Experimental Validation

By constructing a water pump test rig for external characteristic testing, the hydraulic performance of the pump was tested to verify the reliability of the numerical simulations. The obtained flow–head and flow–efficiency characteristic curves from the experiments were compared with the numerical simulation results, as shown in Figure 6c,d. The results revealed that the simulated flow–head curve closely matched the experimental results. As the flow rate increased, the head gradually decreased, and the deviation between the experimental and simulated values also decreased. As for the flow–efficiency curve, the efficiency increased with increasing flow rate and reached its maximum at the design operating point. The efficiency values obtained from the experimental measurements were close to the simulated values. A comparison of the CFD numerical results indicated good agreement between the head and efficiency curves of the mixed-flow pump and the experimental results. The maximum deviation at the design operating point did not exceed 5%, as shown in Table 3, demonstrating the reliability of the computed results.

Table 3. The error of the CFD simulation value and experiment value.

Mass Flow	CFD-H (m)	EXP-H (m)	Error (%)	CFD-η (%)	EXP-η (%)	Error (%)
$0.5Q_{des}$	7.57	7.56	0.11	50.85	51.46	1.19
$0.6Q_{des}$	7.61	7.79	2.26	55.75	53.57	4.07
$0.7Q_{des}$	7.35	7.33	0.31	60.29	60.22	0.13
$0.8Q_{des}$	6.93	6.62	4.57	63.53	62.99	0.85
$0.9Q_{des}$	6.22	6.00	3.80	65.60	65.05	0.84
$1.0Q_{des}$	5.53	5.27	4.98	66.31	65.85	0.71
$1.1Q_{des}$	4.70	4.49	4.67	63.03	61.54	2.43
$1.2Q_{des}$	4.04	3.85	4.86	—	—	—

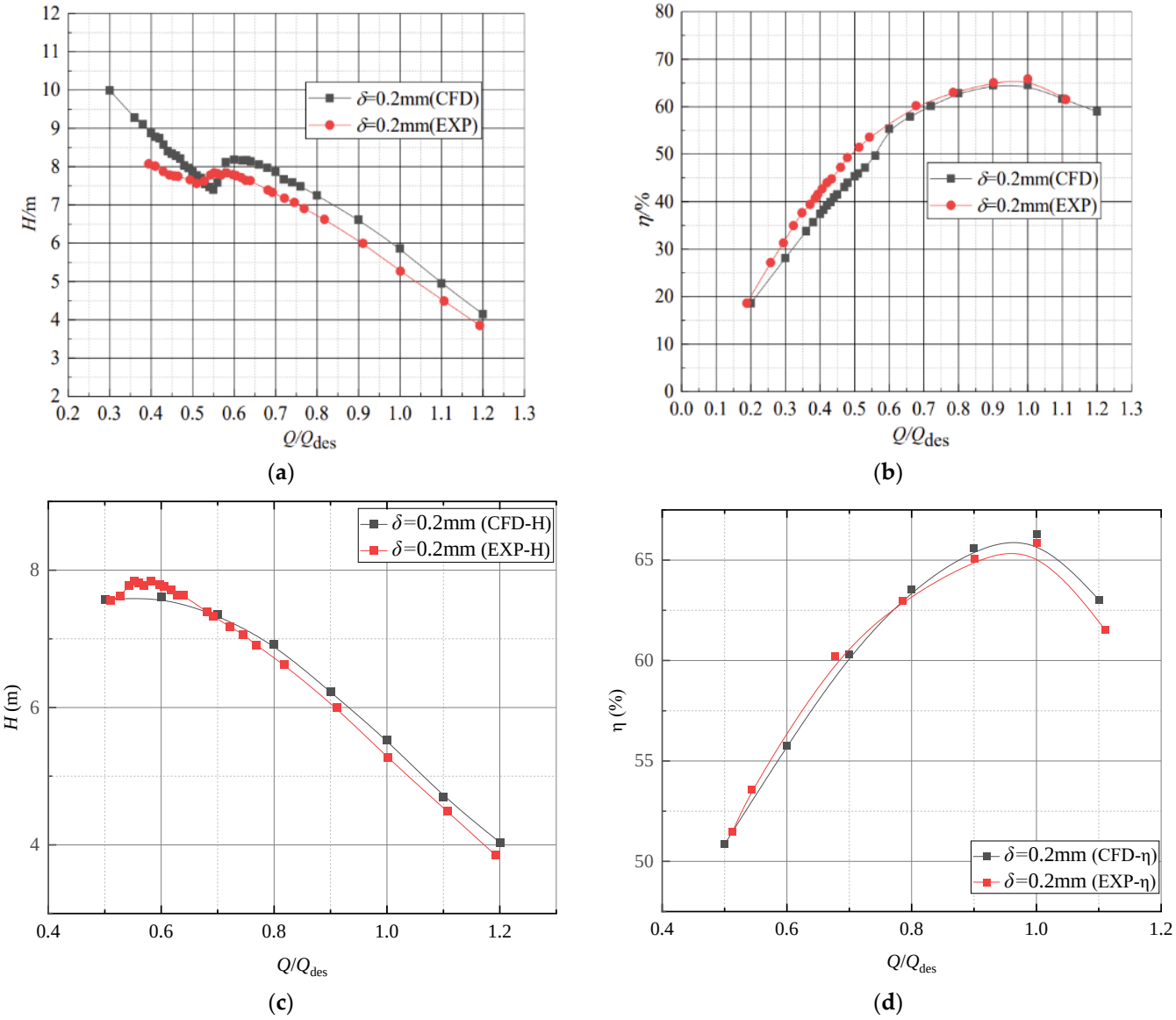

Figure 6. Comparison of experimental and numerical calculation of external characteristics for mixed-flow pump: (**a**) head curve; (**b**) efficiency curve; results of Leilei Ji [35], and (**c**) to (**d**) are the corresponding current study results. These results are in good agreement and hence validate model qualitatively.

In order to validate the current paper simulation model, the current model results are compared qualitatively and quantitatively with the published work [35]. Therefore, the same geometric design is used at the inlet and outlet of the mixed-flow pump, and the meshing is performed in ANSYS ICEM with similar boundary conditions. Figure 2a,b is the published work results. By comparing these results, it is found that they have a good agreement, thus qualitatively verifying the model.

3. Results

3.1. Analysis of the Flow Field Calculation Results

The generation of the internal vortex structure in a mixed-flow pump can significantly affect the internal flow field and energy performance. The flow of viscous fluid is the main cause of vortex generation. In this study, the *Q*-criterion identification method is used to analyze the internal flow of the rotating components and the stationary domain of the mixed-flow pump.

The Q-criterion method is based on the eigenvalue equation of the velocity gradient tensor ∇V.

$$\lambda^3 + P\lambda^2 + Q\lambda + R = 0 \tag{7}$$

If the eigenvalue equation of the velocity gradient tensor ∇V has three eigenvalues λ_1, λ_2, and λ_3, then we have:

$$P = -(\lambda_1 + \lambda_2 + \lambda_3) = -\mathrm{tr}(\nabla V) \tag{8}$$

$$Q = \lambda_1\lambda_2 + \lambda_2\lambda_3 + \lambda_3\lambda_1 = -\frac{1}{2}\left[\mathrm{tr}\left(\nabla V^2\right) + \mathrm{tr}(\nabla V)^2\right] \tag{9}$$

$$R = -\lambda_1\lambda_2\lambda_3 = -\det(\nabla V) \tag{10}$$

where tr is the trace of a matrix; det is the determinant of a matrix; and P, Q, and R are the three Galilean invariants of the velocity gradient tensor ∇V.

Hunt et al. proposed to identify the region with $Q > 0$ as the vortex region. The expression for Q is as follows:

$$Q = \frac{1}{2}\left(\|F\|_F^2 - \|C\|_F^2\right) \tag{11}$$

where F represents the Frobenius paradigm of the matrix; C is the symmetric part of the velocity gradient tensor and F is the antisymmetric part, which corresponds to the deformation and rotation in the flow field, respectively. The advantage of the Q-criterion is the constraint on the ability of the antisymmetric tensor to rotate rigidly in the vortex structure and the rigid rotation of this portion of the antisymmetric tensor to overcome the counteracting effect caused by the deformation of the symmetric tensor. A region satisfying a positive value of Q and an absolute pressure less than 0 is a vortex structure.

Figure 7a shows the vortex structure identified by the Q criterion in the impeller basin, where the threshold value of Q is selected as 500,000 s^{-2}. The impeller, as a strongly rotating component in the mixed-flow pump, is highly susceptible to vortex structure at the impeller inlet by the accelerated rotation. Under four flow conditions, there is a large area of leakage vortex in the rim area, and the leakage vortex is mainly categorized into two types, primary rim leakage vortex (PTLV) and secondary rim leakage vortex (STLV). PTLV is mainly distributed in the main flow path, initially generated in the leading edge, and then develops in the flow path, and develops to the lower vane pressure surface; STLV is mainly distributed in the vicinity of the rim gap area in the form of dispersed strips. At the same time, the rim leakage vortex is disturbed by other vortices, and low-energy fluid accumulates at the trailing edge, forming a trailing edge vortex; the impeller of the mixed flow pump has a more twisted impeller blade shape and a larger vane attached surface layer, which also leads to the generation of a trailing edge vortex. This trailing edge vortex will cause oscillation and pressure pulsation, thus increasing the noise.

The vortex (LE vortex) in front of the blade suction decreases with an increase in the flow rate and completely disappears at the $1.2Q_{des}$ operating condition. Primary rim leakage vortex and secondary leakage vortex always exist; the primary rim leakage vortex area gradually increases with an increase in flow rate and gradually get close to the pressure surface of the next level of blade; while the secondary rim leakage vortex has been in the middle and back section of the rim, and the occupied area basically remains unchanged. The shedding vortex (A) appeared at the $0.8Q_{des}$ operating condition and was most obvious at the $1.0Q_{des}$ operating condition. Meanwhile, a small amount of leakage vortex (B) appeared on the pressure surface rim of the next stage blade at the $1.0Q_{des}$ condition and developed completely at the $1.2Q_{des}$ condition. The trailing edge vortex was most pronounced at the $0.6Q_{des}$ condition and gradually decreased with increasing flow rate.

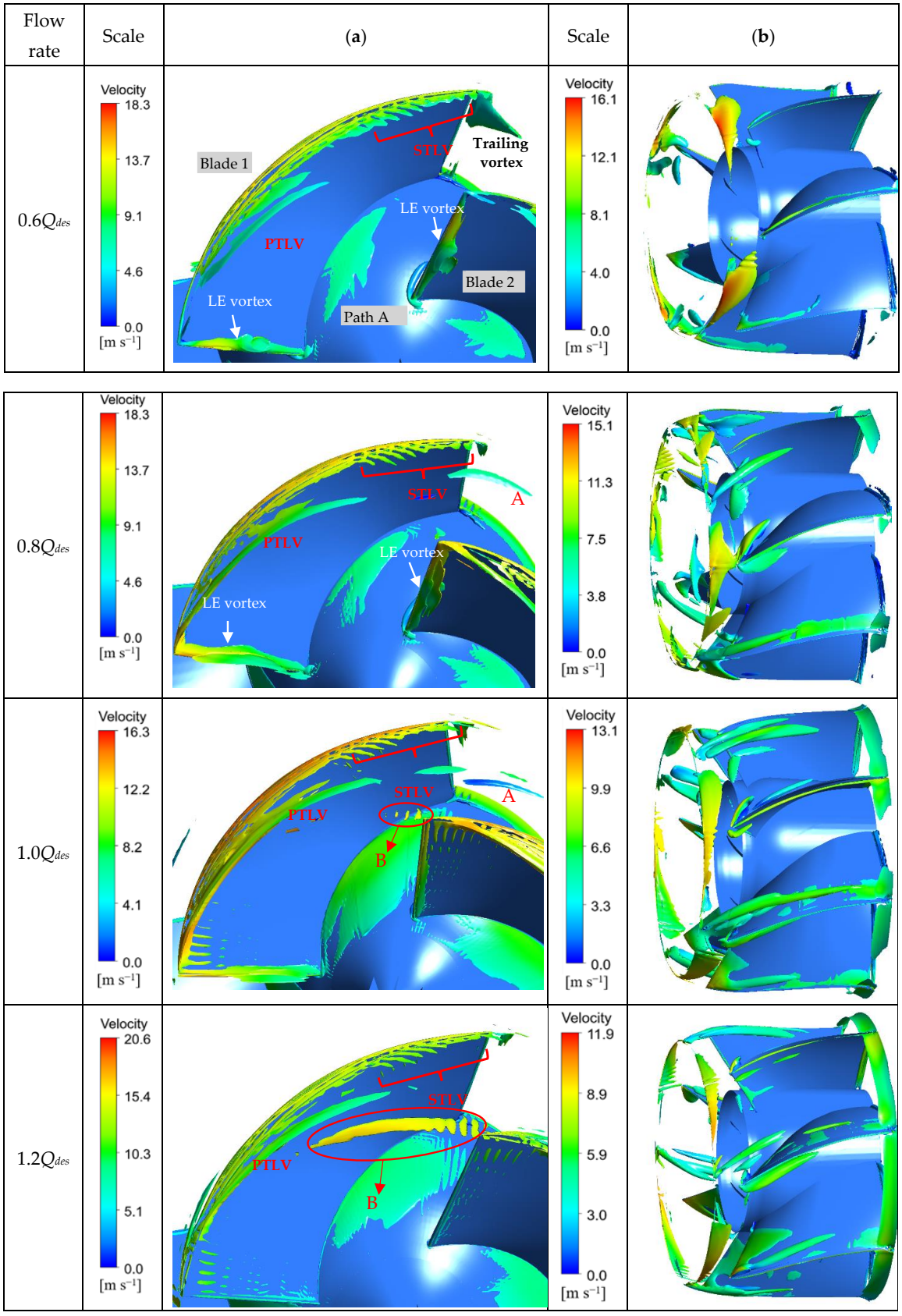

Figure 7. Characteristics of flow field in different flow conditions: (**a**) *Q*-criterion blade vortex diagram; (**b**) *Q*-criterion guide vane vortex diagram.

Figure 7b shows the vortex structure identified by the Q criterion in the guide vane basin, where the threshold value of Q is chosen to be 50,000 s^{-2}. There are two kinds of vortex structures in the guide vane basin; one is the guide vane channel vortex, which develops from the inlet vortex of the guide vane blades and is mainly in the form of a long vortex band, close to the edge of the guide vane wheel, and the guide vane blade shape is more gentle than that of the impeller blade, with a large space in the channel, and the blades have less influence on the evolution of the guide vane channel vortex, which will develop along the channel all the way to the tailpipe. Channel vortex will be along the channel in relation to the tail pipe development, another imported vortex, which is affected by the impeller and guide vane static and dynamic interference and impeller trailing edge of the shedding vortex.

At the $0.6Q_{des}$ condition, there is a large area of inlet vortex and a small amount of vortex structure in the leading and trailing edges of the guide vane; with an increase in the flow, the area of inlet vortex gradually reduces and the speed gradually reduces and shows a strip trend; the vortex structure at the leading edge of the guide vane gradually develops into the vortex of the guide vane channel and extends to the trailing edge, and the guide vortex of the guide vane channel is the most obvious at the condition of $0.8Q_{des}$ and gradually decreases with the increase in flow from $0.8Q_{des}$ to $1.2Q_{des}$. The vortex at the leading edge of the guide vane gradually develops into a vortex at the trailing edge and extends to the trailing edge; the vortex of the guide vane channel is most obvious at the $0.8Q_{des}$ working condition, and from $0.8Q_{des}$ to $1.2Q_{des}$, the vortex of the guide vane channel decreases with the flow rate increase; the vortex structure at the trailing edge develops with the flow rate increase, and it almost connects to a complete annular vortex belt at $1.2Q_{des}$, which is probably caused by the annular volute.

3.2. Analysis of the Acoustic Field Calculation Results

3.2.1. Calculation of Hydrodynamic Noise in Stationary Components

Figure 8 shows the spectrum of the sound pressure level at the inlet and outlet of the pump for four different flow conditions. From the graph, it can be observed that the inlet and outlet sound pressure levels exhibit distinct peaks at the blade passing frequency and its higher harmonics, and the noise frequencies are primarily concentrated in the low-frequency range. Overall, in the high-frequency range, the sound pressure level at the inlet of the pump is significantly higher than that at the outlet. This is mainly because the inlet position of the pump is closer to the region of dynamic and static interference. Additionally, as the flow rate increases, the difference in the sound pressure level between the inlet and outlet gradually decreases. However, in the low-frequency range, the sound pressure levels at both positions are relatively similar.

Figure 9 shows the comparison of sound pressure levels at the inlet and outlet of the pump under different flow rates. From the graph, it can be observed that at the flow rate of $0.6Q_{des}$, both the inlet and outlet sound pressure levels are higher than those at the other three flow rates. This is mainly due to the more complex flow state at the $0.6Q_{des}$ condition, where the swirling at the inlet edge of the guide vane is more pronounced, leading to intensified unstable flow and higher sound pressure levels. As the flow rate increases from $0.8Q_{des}$ to $1.2Q_{des}$, the vortical structures in the guide vane passage and at the trailing edge of the guide vane develop more fully, resulting in an increasing sound pressure level. However, the sound pressure levels at the flow rates of $1.0Q_{des}$ and $1.2Q_{des}$ are essentially the same. At the flow rate of $0.8Q_{des}$, the sound pressure level is the lowest because the wake vortex of the impeller is the smallest in this condition, and the wake vortex has a significant influence on the vortex structure at the inlet of the guide vane, leading to a lower sound pressure level at this flow rate.

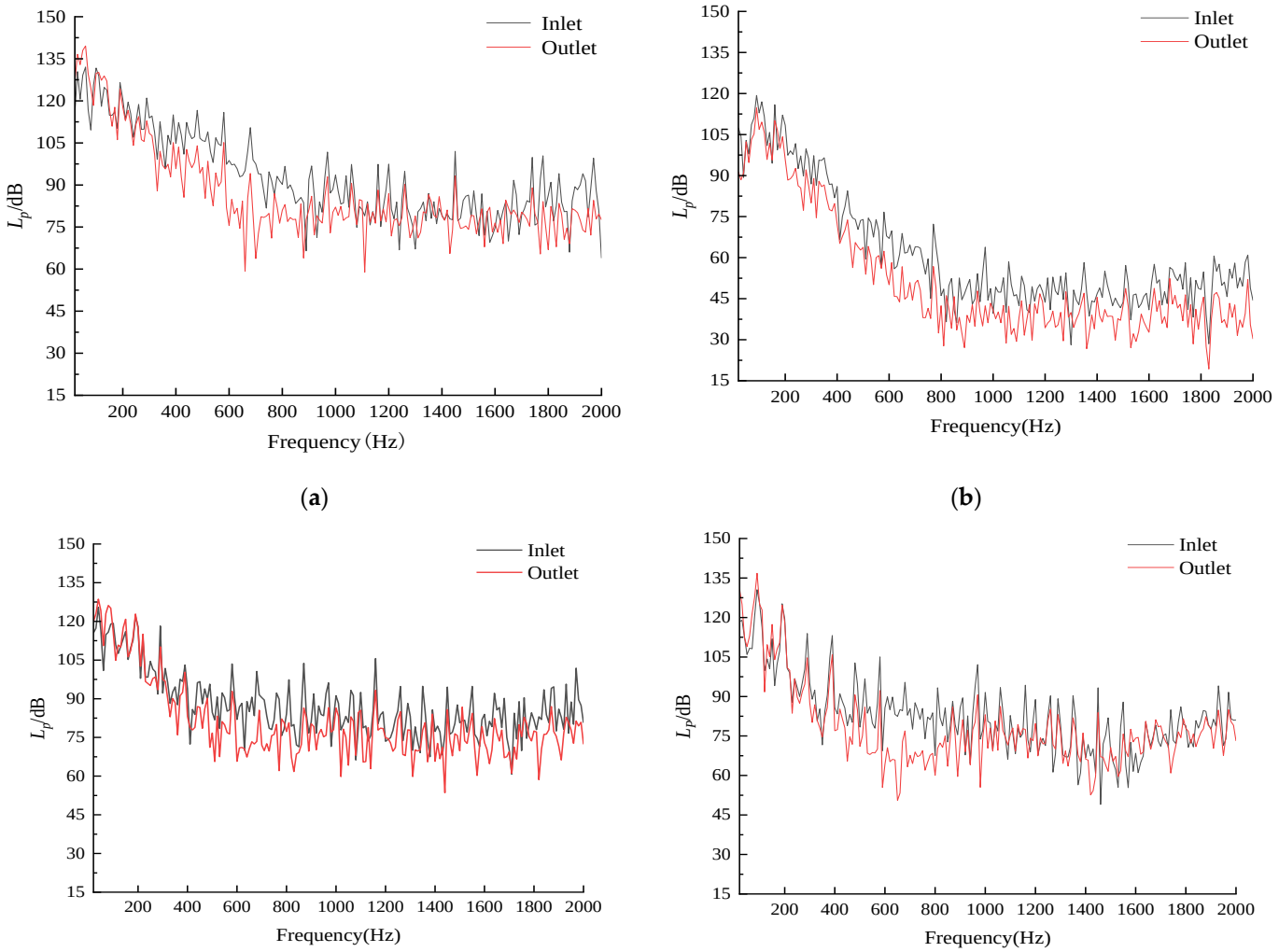

Figure 8. Spectrum of the sound pressure level of the dipole of stationary components under different flow conditions: (**a**) $0.6Q_{des}$; (**b**) $0.8Q_{des}$; (**c**) $1.0Q_{des}$; (**d**) $1.2Q_{des}$.

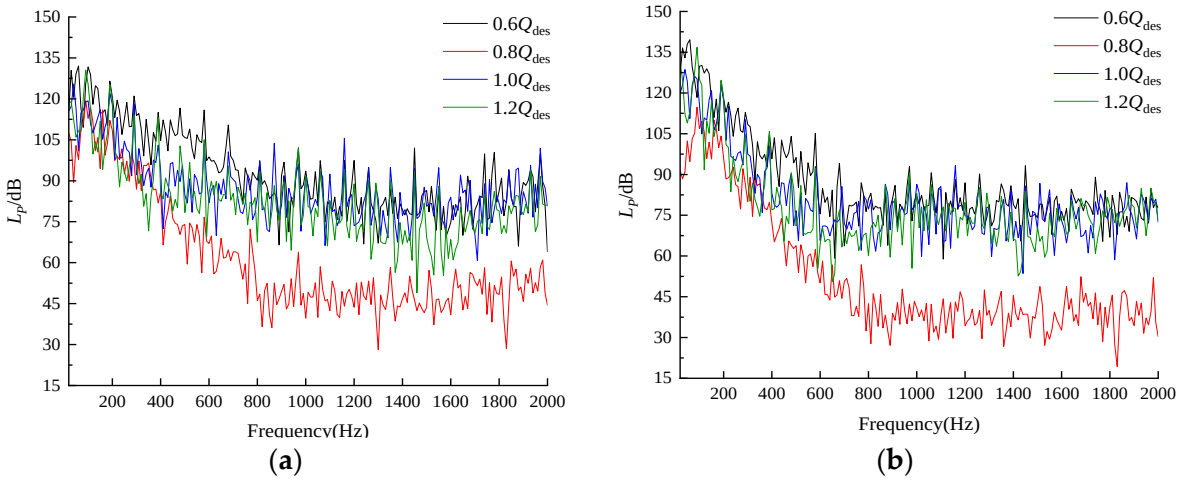

Figure 9. Spectrum of sound pressure level at the inlet and outlet of stationary components: (**a**) pump inlet; (**b**) pump outlet.

Figure 10 shows the contour map of the surface sound pressure level distribution on the internal surface of the stationary component at the first blade passing frequency, obtained from the dipole sound field calculation. It is evident from the graph that the guide vane dipole has a significant impact on the generation of internal noise, while the annular volute has a minor effect on noise generation. In the operating conditions ranging from $0.8Q_{des}$ to $1.2Q_{des}$, as the flow rate increases, the sound pressure level of the stationary component dipole noise at the first blade passing frequency gradually increases and the high-pressure region decreases in size, primarily concentrated at the junction of the impeller and the guide vane. This is because this region is a boundary between the moving and stationary parts, and it experiences wake vortex from the impeller, swirling at the inlet edge of the guide vane, and guide vane passage vortex, resulting in flow instability and noise generation.

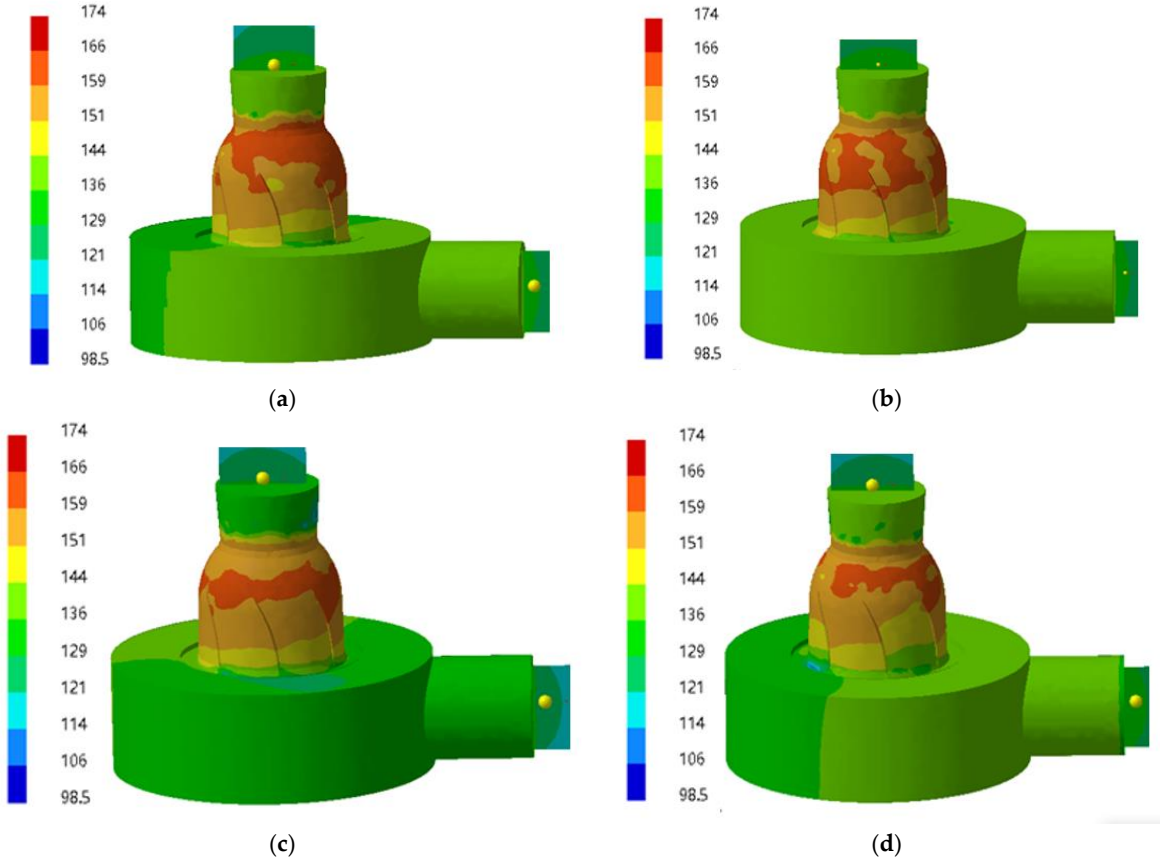

Figure 10. Contours of sound pressure level of stationary component dipole: (**a**) $0.6Q_{des}$; (**b**) $0.8Q_{des}$; (**c**) $1.0Q_{des}$; (**d**) $1.2Q_{des}$.

It can also be seen from Figure 10a that the sound pressure level is higher for the $0.6Q_{des}$ flow condition and the range of the high sound pressure region is larger. Combined with Figure 7b, it can be found that the guide vane inlet vortex is the main cause of noise generation. At the $0.6Q_{des}$ condition, the intensity of inlet vortex is the largest, the vortex area is the largest, and there is no large vortex in the guide vane channel, so the high sound pressure area is mainly concentrated in the leading edge part of the guide vane, which is roughly the same as the vortex volume distribution.

From Figure 10b, it can be seen that the guide vane inlet vortex becomes smaller and the guide vane channel vortex increases in the $0.8Q_{des}$ condition, so the high sound pressure region is more dispersed and moves downward, and the area of the medium sound pressure region is also gradually increased. Compared with the $0.6Q_{des}$ condition,

the sound pressure level decreases, which is because the guide vane inlet vortex has a greater effect on the noise generation.

From Figure 10c,d, it can be seen that at $1.0Q_{des}$, both the guide vane inlet vortex and the guide vane channel vortex are further developed, so the overall sound pressure level increases. At $1.2Q_{des}$, the overall sound pressure level increases further, and the high sound pressure area is concentrated at the junction of the impeller and the guide vane and the area decreases, which is due to the fact that the guide vane inlet vortex is mainly concentrated here and is in the shape of a strip, and the area of the low sound pressure area decreases, which is probably caused by the disappearance of the guide vane channel vortex.

3.2.2. Calculation of Hydrodynamic Noise in Rotating Components

Figure 11 illustrates the frequency spectra of sound pressure levels for the rotating dipole noise at the pump's inlet and outlet under four different flow conditions. The graph reveals distinct peaks in the sound pressure levels at both the pump's inlet and outlet, corresponding to the lobe frequency and its higher harmonic components. However, the primary energy of the noise is predominantly concentrated in the low-frequency range. In the low-frequency range, there is minimal disparity in the sound pressure levels between the pump's inlet and outlet positions. Conversely, in the high-frequency range, the sound pressure level of the noise component at the inlet position significantly surpasses that at the outlet position. As the flow rate increases, phenomena such as flow separation and secondary flow in the impeller channel become less prominent, resulting in a decreasing trend in the sound pressure level of the secondary lobe frequency component.

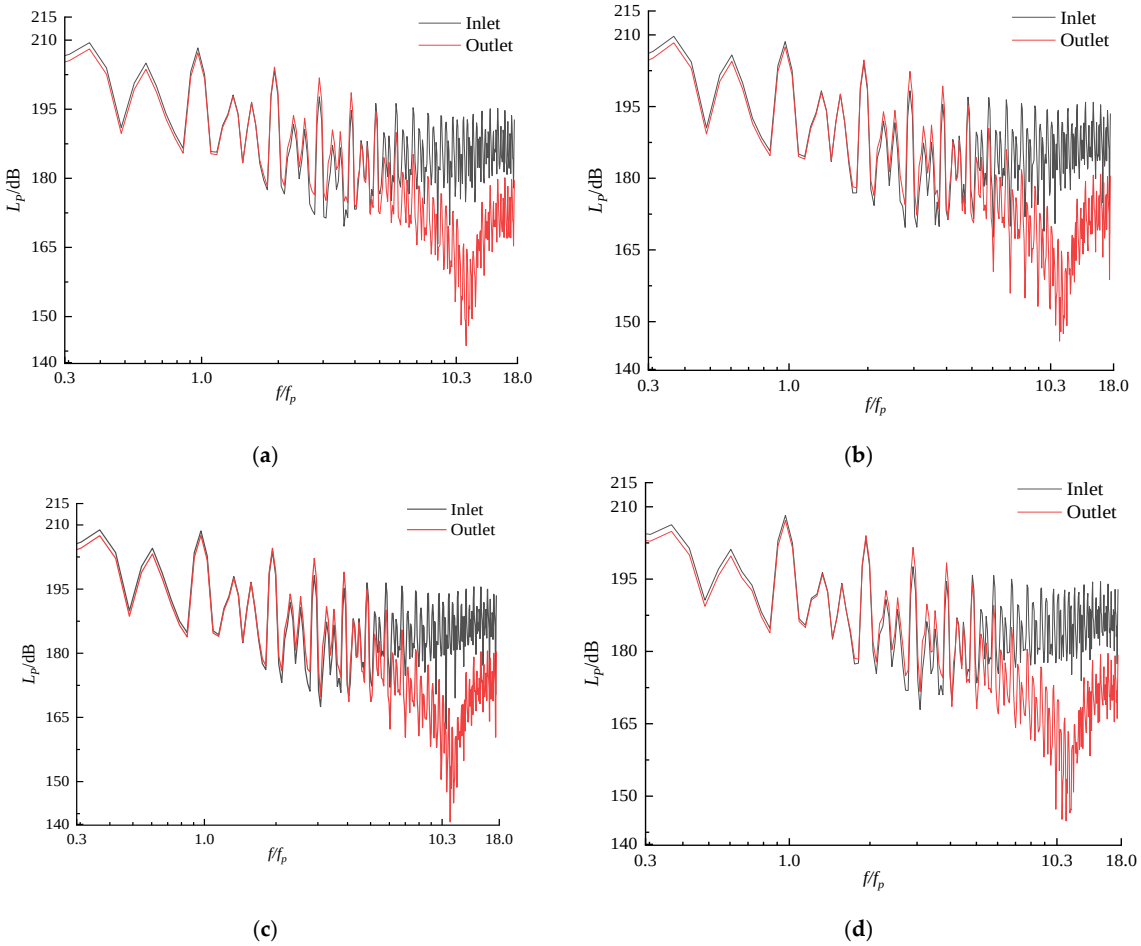

Figure 11. Spectrum of sound pressure level of dipole of rotating components for different flow rate conditions: (**a**) $0.6Q_{des}$; (**b**) $0.8Q_{des}$; (**c**) $1.0Q_{des}$; (**d**) $1.2Q_{des}$.

As evident in Figure 12, the sound pressure levels at the pump's inlet and outlet exhibit a gradual decrease in the higher harmonic frequencies as the flow rate increases. However, in conditions of low flow rates, the sound pressure levels remain relatively stable. Conversely, at the lobe frequency, the differences in sound pressure levels across various flow rates are minimal to the point of being negligible.

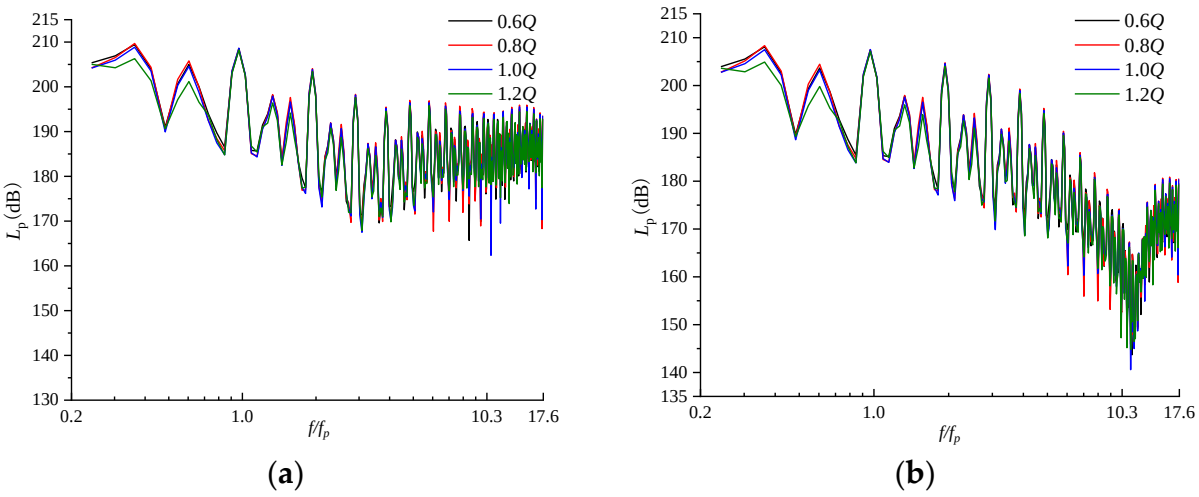

Figure 12. Spectrum of sound pressure level at the inlet and outlet of rotating components: (**a**) pump inlet; (**b**) pump outlet.

Based on the analysis of the flow field, it becomes evident that the impeller's flow state is highly intricate, characterized by the presence of various vortex structures. These vortex structures are responsible for the generation of noise. In conditions of low flow rates, the sound pressure level reaches its peak. This can be attributed to the existence of vortex structures such as flange leakage vortex, impeller leading edge vortex, shedding vortex, and a limited amount of trailing edge vortex in the impeller region. Consequently, the flow state becomes exceptionally complex under these conditions, leading to an unstable flow and an increase in the sound pressure level. As the flow rate increases, there is an improvement in the blade's leading edge vortex and trailing edge vortex. However, the changes in rim leakage vortex are relatively insignificant. This results in a decrease in the sound pressure level, albeit with minimal effect.

Figure 13 presents the frequency-based sound pressure level distribution cloud map of the XY plane field points and the inner surface of the pump casing, obtained from the computational analysis of the rotating component dipole sound field at the first blade-passing frequency. From the figure, it is evident that the sound pressure level cloud map of the impeller dipole exhibits a typical dipole distribution pattern. Furthermore, as the flow rate increases, the range of the intermediate-pressure zone in the XY plane field points gradually expands. A comparison with Figure 10 reveals that the rotating component dipole noise at the first blade-passing frequency is significantly higher than that of the stationary components. This observation highlights the distinctiveness of the dipole noise component generated by the rotating parts compared to the stationary components.

The sound pressure level directivity plot of the impeller dipole noise is shown in Figure 14. From Figure 14, it can be seen that the sound pressure level distribution of the first two orders of the impeller frequency noise component at the position of the directivity field point is a typical dipole distribution. Under the second blade-passing frequency, resonance occurs in the pump body, resulting in significant fluctuations in the sound pressure level. This leads to a noticeably higher sound pressure level at this frequency compared to the sound pressure level at the first blade-passing frequency.

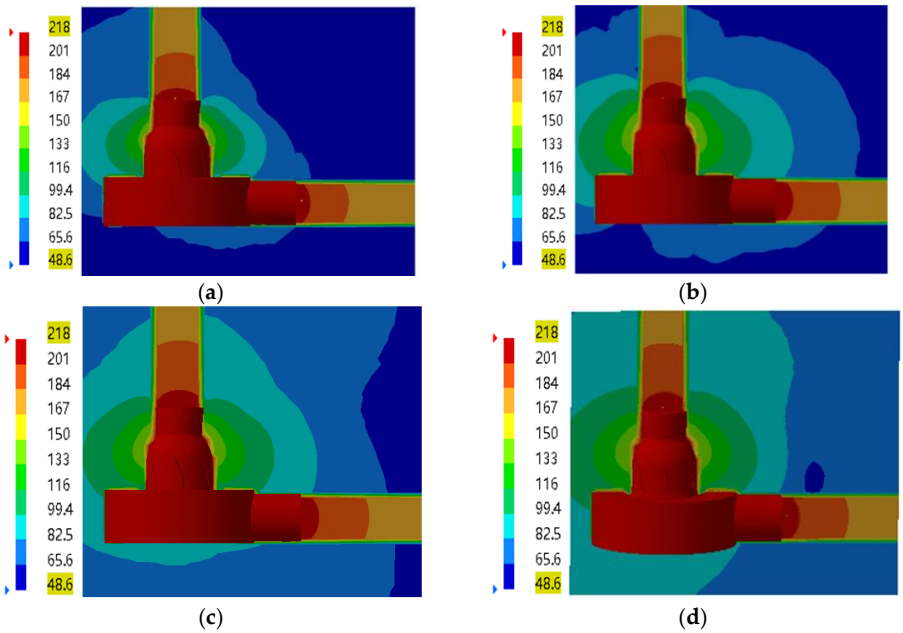

Figure 13. Contours of sound pressure level of rotating component dipole: (**a**) $0.6Q_{des}$; (**b**) $0.8Q_{des}$; (**c**) $1.0Q_{des}$; (**d**) $1.2Q_{des}$.

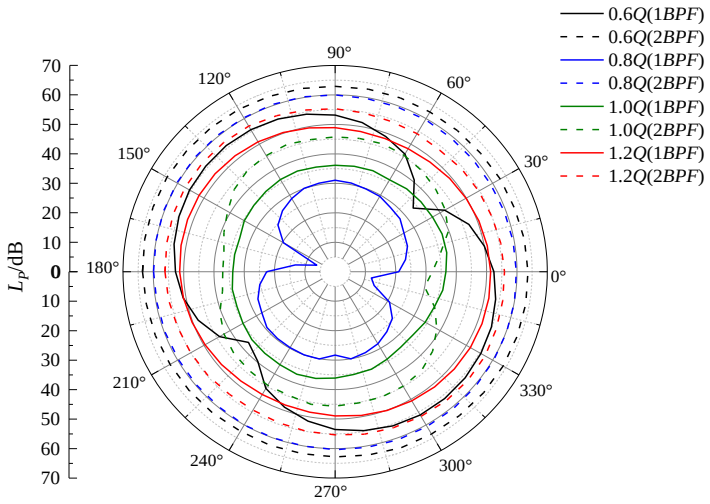

Figure 14. Polar chart of sound pressure level.

3.2.3. Noise Sound Power Comparison

Through the analysis, it can be found that the sound pressure level of the dipole noise of the rotating components is significantly higher than that of the stationary components at the lobe frequency and its harmonic frequency, and the total acoustic energy of the internal sound field of the pump needs to be analyzed uniformly with respect to the sound power level of the two dipole sound sources. Table 4 shows the results of sound power level L_W calculation for hydrodynamic noise of stationary components. Under the design condition, the annular volute as a whole has the lowest sound pressure level and the weakest radiation capability; in comparison, the guide vane has a greater influence on the internal hydrodynamic noise. And the annular volute has an obvious noise reduction effect. Table 5 shows the sound power level L_W calculation results of internal noise. Through the acoustic finite element calculation, the sound power level and the total sound power level of the internal noise of the pump caused by two dipole sound sources under four flow conditions can be obtained.

Table 4. Calculation results of sound power inside stationary components.

Flow Rate	L_W		
	Volute Dipole	**Guide Vane Dipole**	**Stationary Component Dipole**
$1.0Q_{des}$	6.82	87.04	85.00

Table 5. Calculated sound power level of internal noise.

Flow Rate	L_W	
	Stationary Component Dipole	**Rotating Component Dipole**
$0.6Q_{des}$	92.07	167.77
$0.8Q_{des}$	84.95	168.03
$1.0Q_{des}$	85.00	168.08
$1.2Q_{des}$	85.78	167.70

The sound power level spectra of the internal noise of the stationary component dipole and the rotating component dipole are shown in Figure 15. From Figure 15, it is found that the energy of the internal acoustic field due to the two sources is mainly concentrated in the first-order lobe frequency as well as harmonics in the low-frequency range, and the sound power level gradually decreases with increasing frequency. The dipole noise of the stationary component is significantly lower than that of the rotating component under the four flow conditions.

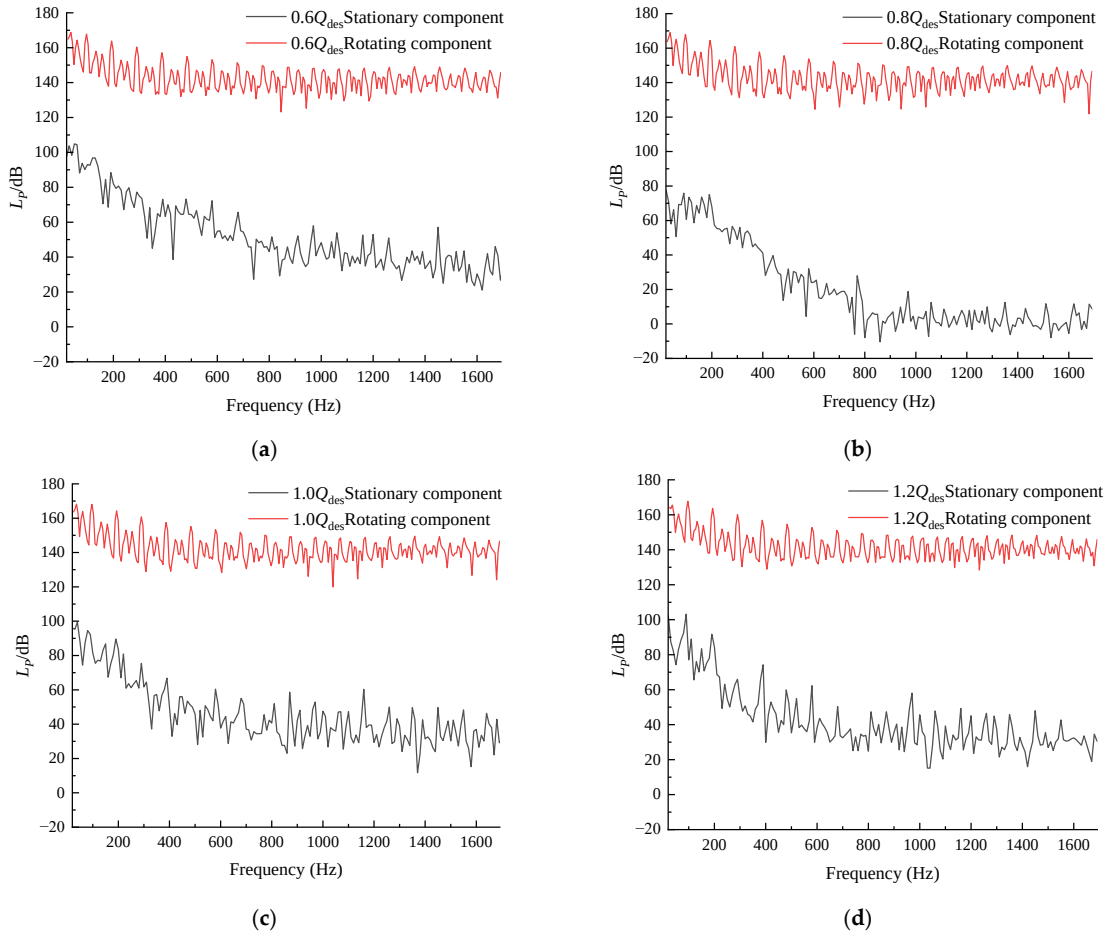

Figure 15. Spectral comparison of sound power level of internal noise: (**a**) $0.6Q_{des}$; (**b**) $0.8Q_{des}$; (**c**) $1.0Q_{des}$; (**d**) $1.2Q_{des}$.

4. Conclusions and Discussion

(1) The internal flow of a mixed-flow pump is complex, with various vortex structures present in the impeller and guide vane domains. The impeller domain exhibits large areas of leakage vortex, while the rim leakage vortex is disturbed by the vortices and accumulates low-energy fluid at the trailing edge, forming a wake vortex. In the guide vane domain, two types of vortex structures exist. One is the inlet vortex, which originates from the dynamic and static interference between the impeller and guide vanes as well as the development of shedding vortices at the impeller trailing edge. The other is the guide vane passage vortex, which evolves from the inlet vortex formed by the guide vane blades. These vortices cause oscillations and pressure fluctuations, thereby increasing noise levels.

(2) Mixed-flow pump internal hydrodynamic noise energy is mainly concentrated in the low-frequency range. The distribution of sound power levels in the frequency spectrum exhibits significant discrete characteristics, with high noise energy amplitudes at the blade passing frequency and its harmonics. Based on the sound power level spectra obtained from four flow conditions, it was observed that the rotating component dipole moments have a significant impact on the internal hydrodynamic noise, while the stationary component dipole moments have a relatively minor influence. Therefore, the internal noise of a mixed-flow pump requires comprehensive consideration of the effects caused by both types of dipole sound sources.

(3) Under the $0.6Q_{des}$ flow condition, the internal flow state of the mixed-flow pump becomes highly complex and unstable. This results in higher sound pressure levels and sound power levels compared to the other three operational conditions. In the flow conditions ranging from $0.8Q_{des}$ to $1.2Q_{des}$, as the flow rate increases, the sound pressure levels gradually increase. Furthermore, the sound pressure levels at the $1.0Q_{des}$ and $1.2Q_{des}$ flow conditions are relatively consistent with each other.

(4) By comparing the sound power levels of the volute dipole and guide vane dipole at the design flow rate, it was found that the volute dipole has a relatively small impact on the internal noise of the mixed-flow pump and even exhibits certain noise reduction effects. This provides insights for noise reduction design in the mixed-flow pump.

The present study provides a detailed comparison with previous works, as outlined in Table 6. The primary focus of this paper is to investigate the impact of flow rate variations on the internal flow field noise in mixed flow pumps and identify the key components influencing hydrodynamic noise in these pumps. These findings offer valuable theoretical support for future efforts in noise reduction for mixed flow pumps. Subsequent research directions include simultaneous consideration of the effects of stationary component dipoles and rotating component dipoles on the hydrodynamic noise in the internal flow field, investigating the coupling between internal and external acoustic fields, and exploring modifications in blade structures to mitigate noise levels.

Table 6. Comparison of the current study with the literature.

Year	Author	Contribution
2016	Jian Fu et al. [10]	They proposed combining the boundary element method with the point sound source model theory and completing the numerical calculation and verification of the static wall flow noise and rotating sound source noise under arbitrary boundary conditions.
2023	Lang Tao et al. [11,12]	They found the characteristics of sound source and aerodynamic noise caused by cavitation in the flow field of single vane pump under different flow conditions.
2023	Si et al. [17]	They developed a three-dimensional flow-acoustic coupling numerical model based on the vortex acoustics equation.
2023	Current study	We have found the variation law of different flow conditions and internal flow noise of the mixed-flow pump and found the main structure affecting the internal flow noise.

Author Contributions: Conceptualization, Q.Y. and W.L.; methodology, Q.Y. and L.J.; software, Q.Y.; validation, W.P., Y.L. and X.H.; formal analysis, Q.Y.; investigation, W.L.; resources, W.L. and W.S.; data curation, L.J.; writing—original draft preparation, Q.Y.; writing—review and editing, Q.Y.; visualization, L.J.; supervision, L.J.; project administration, W.L.; funding acquisition, W.L. All authors have read and agreed to the published version of the manuscript.

Funding: The work was sponsored by the Key International Cooperative research of the National Natural Science Foundation of China (No.52120105010), National Natural Science Foundation of China (No.52179085), National Natural Science Foundation of China (No.52309112), China Postdoctoral Science Foundation (No.2022TQ0127), the Sixth "333 High Level Talented Person Cultivating Project" of Jiangsu Province, funded projects of "Blue Project" in Jiangsu Colleges and Universities, Jiangsu Funding Program for Excellent Postdoctoral Talent (2022ZB667), open research subject of Key Laboratory of Fluid and Power Machinery (Xihua University), Ministry of Education (LTDL-2022010), and the 22nd batch of scientific research projects funded by Jiangsu University (22A231).

Institutional Review Board Statement: Not applicable.

Informed Consent Statement: Not applicable.

Data Availability Statement: The data presented in this study are available on request from the corresponding author.

Conflicts of Interest: The authors declare no conflict of interest.

References

1. Liu, X.; Zhao, D.; Guan, D.; Becker, S.; Sun, D.; Sun, X. Development and progress in aeroacoustic noise reduction on turbofan aeroengines. *Prog. Aerosp. Sci.* **2022**, *130*, 100796. [CrossRef]
2. Smith, T.A.; Rigby, J. Underwater radiated noise from marine vessels: A review of noise reduction methods and technology. *Ocean Eng.* **2022**, *266*, 112863. [CrossRef]
3. Kao, J.-H.; Lin, Y.-J. Predicting the dipole noises of the marine propeller with verifications by experimental measurements. *Ocean Eng.* **2020**, *209*, 107451. [CrossRef]
4. Wu, Q.; Huang, B.; Wang, G.; Cao, S.; Zhu, M. Numerical modelling of unsteady cavitation and induced noise around a marine propeller. *Ocean Eng.* **2018**, *160*, 143–155. [CrossRef]
5. Shi, S.; Huang, X.; Rao, Z.; Su, Z.; Hua, H. Numerical analysis on flow noise and structure-borne noise of fully appended SUBOFF propelled by a pump-jet. *Eng. Anal. Bound. Elem.* **2022**, *138*, 140–158. [CrossRef]
6. Yu, J.; Chen, W.; Zhou, T.; Lee, C.; Huang, X. Transient analysis of trailing edge noise assisted by wavelet-based beamforming and flow visualization. *J. Sound Vib.* **2022**, *526*, 116751. [CrossRef]
7. Stosiak, M.; Karpenko, M.; Prentkovskis, O.; Deptuła, A.; Skačkauskas, P. Research of vibrations effect on hydraulic valves in military vehicles. *Def. Technol.* 2023, *in press*. [CrossRef]
8. Gangipamula, R.; Ranjan, P.; Patil, R.S. Comparative studies on air borne noise and flow induced noise of a double suction centrifugal pump. *Appl. Acoust.* **2023**, *202*, 109148. [CrossRef]
9. Yuan, Z.; Chen, Y.; Mao, X.; Wang, H. Pressure pulsation characteristics and its impact on flow-induced noise in mixed-flow pump. *Trans. Chin. Soc. Agric. Eng. Trans. CSAE* **2015**, *31*, 67–73.
10. Fu, J.; Wang, Y.; Jin, S. Numerical predicting method for hydroacoustics of mixed-flow pump. *J. Cent. S. Univ. (Sci. Technol.)* **2016**, *47*, 62–68.
11. Lang, T.; Sun, Z.; Jin, L.; Chen, K.; Xu, E.; Zhao, J. Analysis of cavitation induced noise characteristics of a single vane centrifugal pump. *J. Drain. Irrig. Mach. Eng. JDIME* **2023**, *41*, 873–880.
12. Lang, T.; Jin, L.; Liu, Y.; Chen, K.; Xu, E. Numerical analysis of hydrodynamic noise characteristics of single-blade centrifugal pump. *J. Drain. Irrig. Mach. Eng. JDIME* **2022**, *40*, 541–548.
13. Han, W.; Guo, W.; Xu, D.; Li, R.; Chen, R. Noise characteristics of screw mixed-flow water-jet pump. *J. Drain. Irrig. Mach. Eng. JDIME* **2020**, *38*, 433–438.
14. Luo, X.; Yang, J.; Song, L. Analysis and research on vibration characteristics of nuclear centrifugal pumps at low flow rates. *Energy Rep.* **2022**, *8*, 1273–1282. [CrossRef]
15. Lu, Y.P.; Tan, L.; Han, Y.D.; Liu, M. Cavitation-vibration correlation of a mixed flow pump under steady state and fast start-up conditions by experiment. *Ocean Eng.* **2022**, *251*, 111158. [CrossRef]
16. Li, W.; Huang, Y.; Ji, L.; Ma, L.; Agarwal, R.K.; Awais, M. Prediction model for energy conversion characteristics during transient processes in a mixed-flow pump. *Energy* **2023**, *271*, 127082. [CrossRef]
17. Si, Q.; Ali, A.; Tian, D.; Chen, M.; Cheng, X.; Yuan, J. Prediction of hydrodynamic noise in ducted propeller using flow field-acoustic field coupled simulation technique based on novel vortex sound theory. *Ocean Eng.* **2023**, *272*, 113907. [CrossRef]
18. Tang, Z.; Zhu, G.; Feng, J.; Wu, Y.; Liu, K.; Lu, Q. Influences of start-up mode on the noise characteristics of mixed-flow pump. *Trans. Chin. Soc. Agric. Eng. Trans. CSAE* **2023**, *39*, 34–42.

19. Ali, A.; Si, Q.; Yuan, J.; Shen, C.; Cao, R.; Saad AlGarni, T.; Awais, M.; Aslam, B. Investigation of energy performance, internal flow and noise characteristics of miniature drainage pump under water–air multiphase flow: Design and part load conditions. *Int. J. Environ. Sci. Technol.* **2021**, *19*, 7661–7678. [CrossRef]
20. Karpenko, M.; Stosiak, M.; Šukevičius, Š.; Skačkauskas, P.; Urbanowicz, K.; Deptuła, A. Hydrodynamic Processes in Angular Fitting Connections of a Transport Machine's Hydraulic Drive. *Machines* **2023**, *11*, 355. [CrossRef]
21. Lighthill, M.J. On Sound Generated Aerodynamically I. General Theory. *Proc. R. Soc. Lond.* **1954**, *222*, 1107.
22. Curle, N. The influence of solid boundaries upon aerodynamic sound. *Proc. R. Soc. Lond. Ser. A* **1955**, *231*, 505–514.
23. Williams, J.E.F.; Hawkings, D.L. Sound generation by turbulence and surfaces in arbitrary motion. *Phil. Trans. Roy. Soc.* **1969**, *264*, 321–342.
24. Farassat, F. Linear Acoustic Formulas for Calculation of Rotating Blade Noise. *AIAA J.* **1981**, *19*, 1122–1130. [CrossRef]
25. Goldstei, M. Unified approach to aerodynamic sound generation in presence of solid boundaries. *J. Acoust. Soc. Am.* **1974**, *56*, 497–509. [CrossRef]
26. Bailly, C.; Bogey, C.; Gloerfelt, X. Some useful hybrid approaches for predicting aerodynamic noise. *C. R. Mec.* **2005**, *333*, 666–675. [CrossRef]
27. Powell, A. Theory of Vortex Sound. *J. Acoust. Soc. Am.* **1964**, *36*, 177–195. [CrossRef]
28. Howe, M.S. Contributions to the theory of aerodynamic sound, with application to excess jet noise and the theory of the flute. *J. Fluid Mech.* **1975**, *71*, 625–673. [CrossRef]
29. Howe, M.S. Influence of wall thickness on Rayleigh conductivity and flow-induced aperture tones. *J. Fluids Struct.* **1997**, *11*, 351–366. [CrossRef]
30. Zhang, J.; Huang, Z. Transient flow and noise characteristics of accelerated flow past a hydrofoil with special emphasis on vortex-turbulence-noise interaction. *Ocean Eng.* **2023**, *268*, 113427. [CrossRef]
31. Zhang, N.; Xie, H.; Wang, X.; Wu, B.-S. Computation of vortical flow and flow induced noise by large eddy simulation with FW-H acoustic analogy and Powell vortex sound theory. *J. Hydrodyn. Ser. B* **2016**, *28*, 255–266.
32. Klapwijk, M.; Lloyd, T.; Vaz, G.; Boogaard, M.v.D.; van Terwisga, T. Exciting a cavitating tip vortex with synthetic inflow turbulence: A CFD analysis of vortex kinematics, dynamics and sound generation. *Ocean Eng.* **2022**, *254*, 111246.
33. Guo, C.; Gao, M.; Wang, J.; Shi, Y.; He, S. The effect of blade outlet angle on the acoustic field distribution characteristics of a centrifugal pump based on Powell vortex sound theory. *Appl. Acoust.* **2019**, *155*, 297–308.
34. Glegg, S.; Devenport, W. Chapter 7—Vortex Sound. In *Aeroacoustics of Low Mach Number Flows*; Glegg, S., Devenport, W., Eds.; Academic Press: Cambridge, MA, USA, 2017; pp. 137–162.
35. Ji, L. *Flow Characteristics and Instability Suppression of Tip Leakage Flow in a Mixed-Flow Pump under Stall Condition*; Jiangsu University: Zhenjiang, China, 2022. [CrossRef]